Widespread distribution of OH/H_2O on the lunar surface inferred from spectral data

Joshua L. Bandfield[1], Michael J. Poston[2], Rachel L. Klima[3], and Christopher S. Edwards[4]

[1]Space Science Institute
[2]California Institute of Technology
[3]Applied Physics Laboratory, Johns Hopkins University
[4]Northern Arizona University

Manuscript Correspondence:

Joshua Bandfield
Space Science Institute
4750 Walnut Street, Suite 205
Boulder, CO 80301, USA

jbandfield@spacescience.org

Abstract

Remote sensing data from lunar orbiters have revealed spectral features consistent with the presence of OH or H_2O on the lunar surface. Analyses of data from the Moon Mineralogy Mapper spectrometer onboard the Chandryaan-1 spacecraft have suggested that OH/H_2O is recycled on diurnal timescales and persists only at high latitudes. However, the spatial distribution and temporal variability of the OH/H_2O, as well as its source, remain uncertain. Here we incorporate a physics-based thermal correction into analysis of reflectance spectra from the Moon Mineralogy Mapper and find that prominent absorption features consistent with OH/H_2O can be present at all latitudes, local times, and surface types examined. This suggests the widespread presence of OH/H_2O on the lunar surface without significant diurnal migration. We suggest that the spectra are consistent with the production of OH in space weathered materials by the solar wind implantation of H^+ and formation of OH at crystal defect sites, as opposed to H_2O sourced from the lunar interior. Regardless of the specific composition or formation mechanism, we conclude that OH/H_2O can be present on the Moon under thermal conditions more wide-ranging than previously recognized.

There is considerable interest in the spectral response of the lunar surface near 3 μm, where OH and H_2O have prominent absorptions. Previous studies have identified these absorptions with variable strengths across the lunar surface[1–8], and have been found to be most prominent at higher latitudes and at early and late local times[1,2,4,8]. These data have led investigators to propose an environment where much of the OH/H_2O migrates around the Moon on diurnal timescales and only persists at high latitudes[1,8]. However, these spectral investigations are based on data that have significantly and variably underestimated lunar surface temperatures and emitted radiance, resulting in significant inaccuracies that can diminish or even entirely eliminate the OH/H_2O related-spectral features around the 3 μm region. Using an updated physics-based thermal correction, we show here that the newly corrected spectral data have a prominent 3 μm absorption that can be present at a range of latitudes, local times, and surface types, suggesting a much more widespread presence of OH/H_2O on the lunar surface. This implies a solar wind source for the OH/H_2O and negates the need for a dynamic migration across the lunar surface on diurnal timescales.

Updated M^3 Spectral Data

A surface roughness and thermal emission model[9,10] (see Methods) was applied to remove thermal contributions to Chandrayaan-1 Moon Mineralogy Mapper (M^3) near-infrared spectra. This model has been validated using Lunar Reconnaissance Orbiter Diviner Radiometer data[10] and is a fundamentally different approach than previously developed thermal corrections, which assumed an empirical relationship between reflectance at specific wavelengths and an isothermal surface[7,11], or derived surface temperatures from spectral measurements at wavelengths near 4 μm[2].

The Diviner measurements closely match the newly developed model, with increasing brightness temperatures at decreasing wavelengths in response to an anisothermal rough lunar surface[10]. The modeled brightness temperatures derived from this work are systematically higher than the M^3 Level 2 data product derived surface temperatures, broadly consistent with other studies[4,7]. The higher

temperatures result in a higher thermal emission contribution to the measured radiance and, consequently, lower reflectance values and a deeper "tail" at 3 μm in the corrected data (Fig. 1).

At wavelengths greater than ~2.75 μm, the corrected reflectance spectra show a prominent negative slope with increasing wavelength. For highlands surfaces, the relative depth of the feature varies by ~20%, with a consistent absorption depth at all angles of solar incidence, despite their wide-ranging conditions (the magnitude of the thermal emission correction at 3 μm varies by a factor of >100). By comparison, the previously released M^3 Level 2 thermally corrected data[11] only show this prominent negative slope at high angles of solar incidence, both at high latitudes and near sunrise and sunset (Fig. 2; Fig S1). We only report the data here in terms of relative 3 μm band strength, which is correlated with OH/H_2O abundance. Particle size/texture and the presence of highly absorbing, opaque phases also influence the magnitude of spectral absorptions, and numerous simplifying assumptions are necessary to quantify OH/H_2O abundance[12–14].

The newly corrected data have also been applied to different surface types (Supplementary Table 1) to identify any spectral dependence on composition or degree of space weathering. Similar to the spectra shown in Fig. 2, small, but systematic differences in band strength are present. In all cases (including many additional locations not reported here), the differences are small relative to the overall strength of the 3 μm absorption and can be comparable in magnitude to the uncertainties in the correction. However, in every case examined with our method, regardless of surface type, latitude, or local time, a prominent 3 μm absorption is present.

For example, the central peak of Bullialdus Crater has a 3 μm absorption similar in depth to that of the crater floor. The central peak has a more prominent minor absorption present near 2.82 μm consistent with previous work[6] (Fig. 3). The strength of the 2.82 μm feature is unchanged by the updated thermal correction, mainly because the spectrally broad thermal emission does not modify the narrow spectral feature. By contrast, the relative depth of the 3 μm feature is significantly different in

the newly corrected data and the updated brightness temperatures average 46 K warmer throughout the area (Fig. S2). In the original Level 2 M^3 data there is a correlation of a deeper 3 μm absorption with the central peak. This correlation disappears with the updated correction (Fig. S2, S3) and the prominent 3 μm absorption is present in the entire area examined.

The methods applied here often predict higher temperatures and emitted radiance near 3 μm than previous results[1,2,7,11], especially at low angles of solar incidence where surfaces are warmest. The correction for higher amounts of emitted radiance for warmer surfaces results in a more prominent and consistent lunar OH/H_2O absorption. For example, previous results using data returned from the Deep Impact - EPOXI mission show lunar 3 μm absorptions with widely varying strength[2]. This apparent inconsistency with the results we present here is likely due to the different methodologies used to derive surface temperatures. In this example, surface temperatures were derived directly from radiance measurements near 4 μm, where emitted radiance is dominant[2]. Using this methodology, both non-unit emissivity near 4 μm and anisothermality due to surface roughness can result in lower ~3 μm brightness temperatures (and less modeled emitted radiance) than predicted by our model.

The high albedo "swirl" features at Reiner Gamma are correlated with a less prominent 3 μm absorption. A similar trend with the 3 μm bands and albedo is present in M^3 data covering the swirl feature at Mare Ingenii (Fig. 4). In Tsiolkovskiy Crater and Oceanus Procellarum, there is a slightly more prominent 3 μm absorption present in the lower albedo maria relative to anorthositic highlands materials, showing a similar relationship as the lunar swirls in absorption strength with respect to albedo (Fig. S4). Although we suggest that there may be systematic trends in the depth of the 3 μm feature with swirl or other albedo features, these differences are relatively small and the 3 μm feature is prominent in all cases examined.

Low albedo mantled surfaces have been identified in numerous locations on the Moon and have been interpreted to be pyroclastic deposits resulting from explosive volcanism[15]. The relatively high

volatile content required for the production of explosive volcanic products suggests the possibility of elevated magmatic OH/H_2O in these materials, which would result in more prominent spectral absorptions near 3 μm[16]. We surveyed three of the larger deposits, Aristarchus Plateau, Sinus Aestuum, and Sulpicius Gallus. Although small differences are present in the relative depth of the 3 μm absorption, these pyroclastic deposits also show consistent 3 μm bands similar in strength to other lunar terrains (Fig. S5).

The final location that we highlight here, the Gruithuisen domes, are an example of lunar silicic volcanism, identified based on their unusual morphological and spectral characteristics[17–20]. Despite the significant differences in bulk composition and mineralogy, the newly-corrected M^3 spectra show no systematic difference in the strength of the 3 μm absorption (Fig. 3). This implies that the silicic surfaces likely have OH/H_2O contents similar to other lunar terrains, though small differences may still be present and not detected via remote spectroscopy. The Gruithuisen domes represent only one of several lunar high silica locations, including some interpreted to be plutonic[19], and a more thorough investigation could help establish any relationship between OH/H_2O content and silicic compositions on the Moon.

Compositional Interpretation

Incorporation of the roughness emission model causes a dramatic change in the depth of the 3 μm absorption in the M^3 reflectance spectra. Previous M^3 results show a prominent 3 μm feature only at cold locations with high solar incidence angles[1,4]. Our work shows deep 3um band features at all locations, regardless of solar incidence angle. This absorption is prominent in all 44 examples listed in Supplementary Table 1, including all lunar surface types and at all latitudes and local times. Given the extreme illumination and temperature ranges for the spectra shown in Fig. 1 (incidence angles of 12–84°; 3 μm brightness temperatures of 275–385 K), it is remarkable how little variation in band depth is present. What variation is present is at the level of uncertainty in the correction method and could be

the result of environmental effects. For instance, the possibility of high vertical thermal gradients could negate the validity of Kirchhoff's Law, however, all existing thermal corrections currently assume Kirchhoff's Law holds (see Methods).

The albedo anomalies known as swirls are a location where there may be a systematic variation in the 3 μm feature. A leading hypothesis for swirl formation is solar wind shielding by crustal magnetic anomalies[5,21–23], which would lead to decreased space weathering and OH/H_2O production in the shielded locations, and consequently a weaker 3 μm absorption. Consistent with previous results indicating that the bright materials are less weathered[21], our data retain a weak trend of high albedo features systematically containing a weaker 3 μm feature than the surrounding dark terrain. Based on this correlation, a latitudinal trend is expected and is also present, though weak, in our results (Fig. 2). Since the variations in 3 μm depth associated with the swirls and latitudinal trends are similar in magnitude to the uncertainty of our correction, additional work is needed before firm conclusions can be drawn on the relationship of the 3 μm feature and space weathering.

The 3 μm feature is typically attributed to the presence of OH/H_2O, but without specifying the precise chemical nature of the "hydration". Changes in the local bonding environment can shift the locations of features, complicating interpretation[24]. For instance, adsorbed OH and H_2O can be present and quite stable in the case of OH attached to crystal defect sites. OH and H_2O can also be dissolved in glasses and H_2O can be present in fluid inclusions and vesicles. Both OH and H_2O can also be present in minerals, both structurally and non-structurally[24].

The dominance of the 3 μm feature can be interpreted as a lunar surface with enhanced H_2O as compared to OH – a somewhat unexpected result, given that OH is thought to be much more readily produced via solar wind implantation and H_2O might only be produced in small concentrations[25]. Although there is a clear dependence of the stability of adsorbed OH and H_2O on surface temperatures[26–28], some studies show that without readsorption or a source of replenishment, the

surfacial H_2O becomes quickly depleted and has a strong dependence on composition[26,27,29]. The high sensitivity of adsorbed H_2O to temperature and composition in the laboratory suggests that if the lunar 3 μm absorption is due to H_2O, it is more tightly bound, possibly as adsorbed H_2O at higher energy sites than observed in the laboratory.

There is an alternate explanation for the presence of the lunar 3 μm absorption. It has been shown that H^+ bombardment of lunar samples can produce broad OH absorptions near 3 μm wavelengths, similar to the M^3 lunar spectra[30]. Ion bombardment has a self-reinforcing effect in that it damages crystals, producing additional high retention energy defect sites with which the H^+ can be bonded[31,32]. The resulting OH species would be in a variety of defect sites, and thus result in a broadened band compared to spectra of materials containing (for example) OH formed in a cooling melt. The 3 μm absorption in the laboratory measurements of space weathered materials, with poorly crystalline and amorphous rims, is much broader and extends to longer wavelengths than that of more crystalline materials[30]. The potential variety of the shape, width, and wavelength of the OH absorption makes interpretation of the specific presence of OH or H_2O based on the wavelength of absorption minima ambiguous[4,33]. As a result, lunar OH may have multiple independent and overlapping absorptions. The broad absorption present near 3 μm in the M^3 data may be due to solar wind implantation of H^+ and formation of OH in space weathered materials, while any other absorptions present, such as the 2.82 μm OH absorption, may result from OH trapped from the melt and bound to crystalline materials[30]. The relatively homogeneous nature of the poorly crystalline space weathered materials in lunar regolith is consistent with the ubiquity of the 3 μm absorption (due to OH formation) across all lunar terrains.

The correlation of the strength of the 3 μm absorption with the intensity of solar wind flux within lunar swirl features (although near the level of uncertainty), as well as the presence of this feature for all lunar surface compositional units, suggest that solar wind processes are responsible for producing the bulk of the OH/H_2O at the lunar surface. Although variations in OHO/H_2O content with petrology

may be present, they are not necessary to account for the spectral features and their variations.

Petrologic Sources of OH/H_2O

The lack of spectral variation associated with compositional surface types does not entirely preclude a magmatic source of lunar OH/H_2O. Evidence for a magmatic source of water on the Moon has been identified in lunar samples, including OH, which has been identified in lunar glasses and apatites in samples of a variety of compositions[34–36]. Concentrations of magmatic lunar water in minerals and fluid inclusions can be high enough to be detectable via spectroscopic measurements[24] and are not likely to be nearly as temperature dependent as adsorbed OH and H_2O. However, the general lack of correlation of band strength with surface composition suggests that solar wind implantation is the dominant source of OH/H_2O detected via spectroscopic remote sensing.

As an exception, Bullialdus Crater is the only location we investigated that clearly shows variations in the strength of the 2.82 μm feature (Fig. 3) that has been tied to differences in petrology and magmatic water content[6]. Other locations also show no systematic variation in the 3 μm feature, such as at pyroclastic deposits at Ina Crater, Aristarchus Plateau, Sinus Aestuum, and Sulpicius Gallus (Fig. S4)[15], or over the high bulk silica Gruithuisen Domes (Fig. 3)[19]. Unlike other recent work[37], our results show no systematic enhancement in the strength of the 3 μm absorption within pyroclastic deposits. This suggests little or no enhancement in water content associated with these volcanic materials.

By contrast, in the few locations examined, lunar maria show slightly deeper 3 μm absorptions than adjacent highlands surfaces (Fig. S3). We speculate that this difference could be due to a slightly higher concentration of OH formed from H^+ implantation. However, the differences are at the level of uncertainty in the correction, and it is also possible that the difference in the strength of the 3 μm absorption reflects variability in magmatic H_2O content of the two lithologies, or simply differences in optical properties of the materials.

Potential for Widespread OH/H2O on the Moon and Airless Bodies

Properly accounting for lunar surface temperatures and roughness reveals a widespread and prominent 3 μm absorption in M^3 data that may be tied to H^+ implantation and formation of OH in poorly crystalline space weathering products. Local variations in the strength of this band are present, but the variations are modest compared to the overall strength of the feature. These variations are also near the limit of uncertainty in the correction method applied to the data. Regardless of the formation process, it appears that OH/H_2O is present on lunar surfaces under conditions much more wide-ranging than previously recognized. The OH/H_2O is either static or in a steady state, without the need for migration across the lunar surface on diurnal timescales.

OH and H_2O derived from H^+ solar wind implantation are likely to be present not only on the Moon, but in general on the surfaces of airless bodies. For example, telescopic observations of small bodies also show spectroscopic evidence for hydration[38] and it is important to understand the data-rich lunar case to serve as a sort of baseline for understanding similar, but less complete data returned from other planetary bodies. The observations shown here may be an initial example of the spectroscopic interpretation of the formation of OH/H_2O as a process common to most airless bodies throughout the solar system.

References

[1] Pieters, C. M., et al. Character and Spatial Distribution of OH/H_2O on the Surface of the Moon Seen by M^3 on Chandrayaan-1. *Science*, **326**, 568-572 http://dx.doi.org/56810.1126/science.1178658 (2009).

[2] Sunshine, J. M., et al. Temporal and Spatial Variability of Lunar Hydration As Observed by the Deep Impact Spacecraft. *Science*, **326**, 565-568 http://dx.doi.org/56510.1126/science.1179788 (2009).

[3] Clark, R. N. Detection of Adsorbed Water and Hydroxyl on the Moon. *Science*, **326**, 562-564 http://dx.doi.org/56210.1126/science.1178105 (2009).

[4] McCord, T. B., et al. Sources and physical processes responsible for OH/H_2O in the lunar soil as revealed by the Moon Mineralogy Mapper (M^3). *J. Geophys. Res.*, **116** (E6) http://dx.doi.org/10.1029/2010JE003711 (2011).

[5] Kramer, G. Y., et al. M^3 spectral analysis of lunar swirls and the link between optical maturation and surface hydroxyl formation at magnetic anomalies. *J. Geophys. Res.*, **116** (E6) http://dx.doi.org/10.1029/2010JE003729 (2011).

[6] Klima, R., Cahill J., Hagerty, J., & Lawrence, D. Remote detection of magmatic water in Bullialdus Crater on the Moon. *Nat. Geosci.*, **6**, 737-741 http://dx.doi.org/10.1038/ngeo1909 (2013).

[7] Li, S., & Milliken, R. E. An empirical thermal correction model for Moon Mineralogy Mapper data constrained by laboratory spectra and Diviner temperatures, *J. Geophys. Res.*, **121**, 2081–2107 http://dx.doi.org/10.1002/ 2016JE005035 (2016).

[8] Wöhler, C., A. et al. Temperature regime and water/hydroxyl behavior in the crater Boguslawsky on the Moon. *Icarus*, **285**, 118-136 http://dx.doi.org/10.1016/j.icarus.2016.12.026 (2017).

[9] Bandfield, J. L. & Edwards, C. S. (2008) Derivation of martian surface slope characteristics from directional thermal infrared radiometry. *Icarus*, **193**, 139-157 http://dx.doi.org/10.1016/j.icarus.2007.08.028 (2008).

[10] Bandfield, J. L., P. O. Hayne, P. O., Williams, J-. P., Greenhagen, B. T., & Paige, D. A. Lunar surface roughness derived from LRO Diviner Radiometer observations. *Icarus*, **248**, 357-372 http://dx.doi.org/10.1016/j.icarus.2014.11.009 (2015).

[11] Clark, R. N., Pieters, C. M., Green, R. O., Boardman, J. W., & Petro, N. E. Thermal removal from near-infrared imaging spectroscopy data of the Moon. *J. Geophys. Res.*, **116**, (E6) 10.1029/2010JE003751 (2011).

[12] Clark, R. N. Spectral properties of mixtures of montmorillonite and dark grains - Implications for remote sensing minerals containing chemically and physically adsorbed water. *J. Geophys. Res.*, **88**, 10635-10644 http://dx.doi.org/10.1029/JB088iB12p10635 (1983).

[13] Hapke, B. *Theory of reflectance and emittance spectroscopy* (Cambridge University Press, Cambridge, 1993).

[14] Milliken, R. E. & Mustard, J. F. (2007) Estimating the water content of hydrated minerals using reflectance spectroscopy. I. Effects of darkening agents and low-albedo materials. *Icarus*, **189**, 550-573 http://dx.doi.org/10.1016/j.icarus.2007.02.017.

[15] Gaddis, L. R., Staid M. I., Tyburczy J. A., Hawke, B. R., Petro, N. E. Compositional analyses of lunar pyroclastic deposits. Icarus, **161**, 262-280 http://dx.doi.org/10.1016/S0019-1035(02)00036-2 (2003).

[16] Head, J. W. & Wilson, L. (2017) Generation, ascent and eruption of magma on the Moon: New insights into source depths, magma supply, intrusions and effusive/explosive eruptions (Part 2: Predicted emplacement processes and observations). *Icarus*, **283**, 176-223

10.1016/j.icarus.2016.05.031.

[17] Head, J. W. & McCord, T. B. (1978) Imbrian-age highland volcanism on the moon - The Gruithuisen and Mairan domes. Science, **199**, 1433-1436 http://dx.doi.org/10.1126/science.199.4336.1433.

[18] Wilson, L. & Head, J. W. Lunar Gruithuisen and Mairan domes: Rheology and mode of emplacement. *J. Geophys. Res.*, **108** (E2) http://dx.doi.org/5012-1 10.1029/2002JE001909 (2003).

[19] Glotch, T. D., et al. Highly Silicic Compositions on the Moon. *Science*, **329**, 1510-1513 http://dx.doi.org/151010.1126/science.1192148 (2010).

[20] Ivanov, M. A., Head J. W., & Bystrov, A. The lunar Gruithuisen silicic extrusive domes: Topographic configuration, morphology, ages, and internal structure. *Icarus*, **273**, 262-283 http://dx.doi.org/10.1016/j.icarus.2015.12.015 (2016).

[21] Hemingway, D. J., Garrick-Bethell, I., & Kreslavsky, M. A. Latitudinal variation in spectral properties of the lunar maria and implications for space weathering. *Icarus*, **261**, 66-79 http://dx.doi.org/10.1016/j.icarus.2015.08.004 (2015).

[22] Glotch, T. D. et al. Formation of lunar swirls by magnetic field standoff of the solar wind. *Nat. Communicat.*, **6**, 6189 http://dx.doi.org/618910.1038/ncomms7189 (2015).

[23] Hood, L. L. & Schubert, G. Lunar magnetic anomalies and surface optical properties. *Science*, **208**, 49-51 http://dx.doi.org/10.1126/science.208.4439.49 (1980).

[24] Dyar, M. D., Hibbitts, C. A., & Orlando, T. M. Mechanisms for incorporation of hydrogen in and on terrestrial planetary surfaces. *Icarus*, **208**, 425-437 http://dx.doi.org/10.1016/j.icarus.2010.02.014 (2010).

[25] Bradley, J. P. et al. Detection of solar wind-produced water in irradiated rims on silicate minerals. *Proc. Nation. Acad. Sci.*, **111**, 1732-1735 http://dx.doi.org/10.1073/pnas.1320115111 (2014).

[26] Poston, M. J. et al. Water interactions with micronized lunar surrogates JSC-1A and albite under ultra-high vacuum with application to lunar observations. *J. Geophys. Res.*, **118**, 105-115 http://dx.doi.org/10.1029/2012JE004283 (2013).

[27] Hibbitts, C. A. et al. Thermal stability of water and hydroxyl on the surface of the Moon from temperature-programmed desorption measurements of lunar analog materials. *Icarus*, **213**, 64-72 http://dx.doi.org/10.1016/j.icarus.2011.02.015 (2011).

[28] Mitchell, E. H. et al. Ultraviolet photodesorption as a driver of water migration on the lunar surface. *Planet. Space Sci.*, **89**, 42-46 10.1016/j.pss.2013.02.002.

[29] Poston, M. J. et al. Temperature programmed desorption studies of water interactions with Apollo lunar samples 12001 and 72501. *Icarus*, **255**, 24-29 http://dx.doi.org/10.1016/j.icarus.2014.09.049 (2015).

[30] Ichimura, A. S., Zent, A. P., Quinn, R. C., Sanchez, M. R., & Taylor, L. A. Hydroxyl (OH) production on airless planetary bodies: Evidence from H^+/D^+ ion-beam experiments. *Earth and Planet. Sci. Lett.*, **345**, 90-94 http://dx.doi.org/10.1016/j.epsl.2012.06.027 (2012).

[31] Farrell, W. M., Hurley, D. M., Esposito, V. J., McLain, J. L., & Zimmerman, M. I. The statistical mechanics of solar wind hydroxylation at the Moon, within lunar magnetic anomalies, and at Phobos, *J. Geophys. Res.*, **122**, 269-289 http://dx.doi.org/10.1002/2016JE005168 (2017).

[32] Farrell, W. M., Hurley, D. M., & Zimmerman, M. I. Solar wind implantation into lunar regolith: Hydrogen retention in a surface with defects. *Icarus*, **255**, 116-126 http://dx.doi.org/10.1016/j.icarus.2014.09.014 (2015).

[33] Starukhina, L. Water detection on atmosphereless celestial bodies: Alternative explanations of the observations. *J. Geophys. Res.*, **106**, 14701-14710 http://dx.doi.org/10.1029/2000JE001307 (2001).

[34] Saal, A.E. et al. Volatile content of lunar volcanic glasses and the presence of water in the Moon's

interior. *Nature*, **454**, 192-195 http://dx.doi.org/10.1038/nature07047 (2008).

[35] McCubbin, F. M. et al. Nominally hydrous magmatism on the Moon. *Proc. Nation. Acad. Sci.e*, **107**, 11223-11228 http://dx.doi.org/10.1073/pnas.1006677107 (2010).

[36] Greenwood, J.P. et al. Hydrogen isotope ratios in lunar rocks indicate delivery of cometary water to the Moon. *Nat. Geosci.*, **4**, 79–82 http://dx.doi.org/10.1038/ngeo1050 (2011).

[37] Milliken, R. E. & Li, S. Remote detection of widespread indigenous water in lunar pyroclastic deposits. *Nat. Geosci.*, **10**, 561-565 http://dx.doi.org/10.1038/NGEO2993 (2017).

[38] Rivkin, A. S. et al. 3μm Spectrophotometric Survey of M- and E-Class Asteroids. *Icarus*, **117**, 90-100 http://dx.doi.org/10.1006/icar.1995.1144 (1995).

Acknowledgments

We would like to acknowledge funding by the Lunar Reconnaissance Orbiter program and Lunar Data Analysis Program grant NNX16AN63G. Our work benefited from discussions with the LRO Diviner science team, Shuai Li, and Ralph Milliken.

Corresponding Author

Correspondence and any requests for model results or code should be sent to Joshua Bandfield (jbandfield@spacescience.org).

Author Contributions

J.L.B. developed the thermal correction model and led the processing and analysis of the M^3 and Diviner data.

M.J.P. contributed to the interpretation of spectral features and the development of formation mechanism hypotheses.

R.L.K. contributed to the spectral interpretation of the M^3 data and discussions of petrological sources of OH/H_2O.

C.S.E. contributed to the development of the thermal and roughness model and assisted with the interpretation of the spectral datasets.

Competing Interests

The authors declare no competing financial interests.

Figure Captions

Figure 1. Example spectra showing the effects of various thermal corrections on the shape and depth of the 3 μm absorption. The original uncorrected spectrum (red) and the M^3 Level 2 thermally corrected (blue) spectra show little evidence for a 3 μm absorption. Thermal corrections using radiative equilibrium, but neglecting surface roughness (green) predict surface temperatures comparable to LRO Diviner measurements, but fail to predict the expected higher brightness temperatures at shorter wavelengths present in both Diviner data and the roughness model (cyan). Data are from M^3 image M3G20090125T172601.

Figure 2. Normalized reflectance of lunar highlands surfaces over a range of solar incidence angles (11–84°). The top plot shows spectra corrected for thermal emission using the roughness and thermal emission model with derived 3 μm brightness temperatures from 385 to 275K. The bottom plot shows the M^3 Level 2 thermally corrected data for the same locations with derived surface temperatures of 353 to 0 K (Table S1).

Figure 3. M^3 normalized reflectance spectra of the central peak and crater floor of Bullialdus Crater (top) and Gruithuisen Delta dome (bottom). Despite differences in the prominence of the minor 2.82 μm absorption (denoted by the arrow), the strength of the broad 3 μm absorption is comparable between the two surfaces. The spectra of Guithuisen Delta dome and nearby mare surfaces show similar 3 μm absorptions despite differences in composition and albedo (Table S1).

Figure 4. Reiner Gamma and Mare Ingenii lunar swirl region bright (red) and dark (blue) surface reflectance spectra. Dark surfaces have consistently deeper 3 μm absorptions than bright surfaces within lunar swirl features.

35

Methods

Thermal Emission and Roughness Model: The roughness and thermal emission model predicts the emitted radiance from the lunar surface as a function of wavelength. Surface temperatures for each facet of the rough surface are predicted assuming radiative equilibrium. Sloped surfaces include a downwelling radiative component proportional to the fraction of the hemisphere filled by adjacent surfaces rather than space. The solar and thermal infrared downwelling radiance is calculated assuming it is emitted from a horizontal surface at radiative equilibrium. The assumption of radiative equilibrium is appropriate for lunar daytime surfaces with low thermal inertia (>99% of the surface). Under these conditions, heat diffusion models predict equatorial surface temperatures within ~1 K of radiative equilibrium between 0800H and 1600H.

This model is similar to that described by *Bandfield et al.* (2015)[10], but with several modifications to more realistically predict emitted radiance at high angles of solar incidence. These modifications include solar incidence-dependent albedo and improved cast shadow prediction (described below). The modeled lunar radiance now more closely matches measurements at high angles of solar incidence, where shadowing becomes significant. For this work we use a RMS slope distribution of 20°, similar to previous work[10]. The important aspect of this problem is that the model accurately predicts the range of temperatures present and emitted radiance, not the physical roughness of the surface.

At latitudes <60°, the regional slope and azimuth angles of the surface are derived from the LOLA/Kaguya digital terrain model (DTM)[39]. At higher latitudes, the LRO Camera Global DTM is used[40]. Uncertainties in the location of the M^3 measurements can be several km and the latitude and longitude offset between the M^3 data and the DTM's is determined and manually corrected by identifying recognizable features in both datasets and determining the pixel offset. Due to the imprecision in the alignment between the datasets, topographic features near the scale of the M^3

measurements can be mis-registered. This, combined with the high dependence of surface temperature on local slope orientation, has severe effects on the thermal correction. Consequently, data used for this study avoided sharp topographic boundaries and small craters that could interfere with the thermal correction.

For radiative balance, hemispherical emissivity is assumed to be 0.95 based on LRO Diviner multiple emission angle measurements of daytime surfaces[10]. This value of emissivity is only used to predict surface kinetic temperature and is well characterized based on LRO Diviner measurements, where by far the bulk of emitted radiance occurs. Hemispherical albedo, A_H, is calculated according to the formula[41,42],

$$A_H = A_R + 0.045 \cdot (I_{sun} / 45)^3 + 0.14 \cdot (I_{sun} / 90)^8 \qquad (1)$$

where A_R is the broadband albedo derived from the M^3 reflectance and I_{sun} is the solar incidence in degrees.

Shadowed surface temperatures cannot be determined using radiative equilibrium and are set in the model according to an empirical relationship derived from Diviner multispectral data acquired throughout the lunar day. Where the solar incidence for a given slope angle is greater than 90° or for surfaces within cast shadows (described below), the surface is set to a temperature, T_{shade} as a function of regional solar incidence.

$$T_{shade} = T_{surf} - f \cdot 100 \qquad (2)$$

where T_{surf} is the surface temperature for a level, unshaded surface and f is a multiplicative factor determined from the following:

$$f = 1 - (I_{sun} - 60) / 30 \cdot 0.6 \text{ for local time } <1200\text{H}$$

$$f = 1 - (I_{sun} - 60) / 30 \cdot 0.75 \text{ for local time } >1200\text{H} \qquad (3)$$

$$f = 1 \text{ for } I_{sun}<60$$

In practice, the precise temperature of shaded surfaces matters little for daytime measurements near

3 μm wavelengths because the amount of radiance emitted from cold shadowed surfaces is negligible.

Surface Roughness Model: We use a simple Gaussian roughness model that is similar to that used previously for comparison with martian and lunar surfaces[10,43,44]. The probability distribution P for a given slope angle, θ, is described by the following (derived from Eq. 13 of *Shepard et al.*, 1995[44]):

$$P(\theta) = \frac{\tan(\theta)}{\tan(\theta_0)} \cdot e^{\left(\frac{-\tan^2(\theta)}{2 \cdot \tan^2(\theta_0)}\right)} \quad (4)$$

where θ_0 is the tangent of the RMS slope angle. This describes the adirectional distribution of slopes, which closely approximates a Gaussian distribution of unidirectional slopes for a RMS slope angle of θ_0[44]. For our purpose, the azimuth direction for the slope of any given surface has no preferential orientation and our measurements are sensitive to an adirectional distribution of slopes with random azimuths rather than the slope distribution along any particular transect or orientation.

Surface temperatures are predicted using the model described above for slopes of 0° to 90° at 2° intervals and azimuth orientations of 0° to 360° at 20° intervals. The radiance of each slope/azimuth combination is calculated, and its contribution to the total modeled radiance is weighted by the statistical probability of its occurrence and its projection on the plane orthogonal to the vector defined by the viewing direction. This produces radiance as a function of wavelength and reduces the surface slopes/roughness to a single parameter (RMS slope) that requires no assumption regarding length scales, while maintaining reasonable fidelity to natural surfaces and has been shown to match the multispectral emission from most lunar surfaces[10].

Shadows greatly influence the emitted radiance from planetary surfaces at high angles of solar incidence or where high slope angles are present. Although it is simple to predict whether a sloped surface has a local solar incidence of greater than 90°, predicting the distribution of cast shadows on slopes that would otherwise be sunlit is much more difficult and an exact solution requires ray-casting and other computationally expensive methods.

Although the proportion of a surface containing cast shadows can be closely and simply approximated[45], surfaces that fall within cast shadows are strongly biased towards higher slope angles that face away from the sun. In order to properly account for this bias, the statistical occurrence of cast shadows versus facet orientation was determined using randomly generated digital terrain models with RMS slope distributions from 0–50° and solar incidence angles of 0–90°. These statistics were used to build a lookup table of shadow proportions for each slope and azimuth orientation used in the model.

The inclusion of the ray-tracing-based cast shadowing in this model results in a substantial improvement over previous results[10] in the consistency of retrieved RMS slope distribution values. This is especially the case at high angles of solar incidence, where cast shadows are a significant contribution to the field of view. Previous results showed an apparent decrease in RMS slope distributions at solar incidence angles greater than ~45°[10]. The updated model described here is similar to previous results at low angles of solar incidence, but closely matches the Diviner data using a single RMS slope value across a wide range of solar incidence angles (Fig. S6). The specific value of roughness used strongly influences the predicted surface temperature distributions and can have a dramatic effect on the apparent strength of the 3 μm absorption, even at moderate angles of solar incidence (Fig. S7).

M^3 Data Processing: With the exception of the thermal correction, M^3 data were processed using the methods described in the Data Product Software Interface Specification (DPSIS) available at: http://pdsimage.wr.usgs.gov/Missions/Chandrayaan_1/M3/CH1M3_0003/DOCUMENT/DPSIS.PDF. The calculation of reflectance includes four steps; 1) Conversion of radiance to reflectance factor (I/F); 2) Statistical polishing to remove spectral noise; 3) Thermal emission removal (described below); 4) Photometric correction, including accounting for limb darkening using a Lommel-Seeliger model[46]. Because of the uncertainty in the original thermal correction, the photometric correction (derived from the M^3 measurements), may be a source of uncertainty in the processed M^3 processing pipeline. At

wavelengths less than ~2 μm where thermal emission is negligible on the Moon, reflectance values calculated for this work are identical to the M^3 Level 2 reflectance data products available at the Planetary Data System (PDS).

The correction of M^3 data using the output of the roughness emission model is relatively straightforward. Measured radiance can be approximated by the following:

$$I_{meas} = \frac{R_c F_{sun}}{d^2 \pi} + \varepsilon I_e \quad (5)$$

Where I_{meas} is the calibrated radiance, I_e is the modeled emitted radiance (the weighted mixture of Planck radiance at the modeled temperatures), R_c is the thermally corrected reflectance, F_{sun} is the solar irradiance, d is the solar distance, and ε is the surface emissivity. All terms are wavelength dependent and spectral polishing and photometric corrections are separate multiplicative terms not listed here. By assuming Kirchhoff's Law ($\varepsilon = 1 - R$, where ε is surface emissivity and R is reflectance), Equation 5 can be rearranged and thermally corrected reflectance determined by the following:

$$R_c = \frac{I_{meas} - I_e}{\frac{F_{sun}}{d^2 \pi} - I_e} \quad (6)$$

Similar to other thermal correction methods[7,8,11], we assume that Kirchhoff's Law applies . This assumption is only valid where the surface is vertically isothermal within the penetration depth of the measurement (<100's of μm). Although laboratory work has shown that these extreme temperature gradients can occur in highly insulating materials in a vacuum[47–49], in practice the low spectral contrast present in lunar thermal infrared spectra indicates that these severe thermal gradients are not present on typical lunar daytime surfaces[50,51].

Kirchhoff's Law applies to directional-hemispherical reflectance[52-53]. However, the procedure that we use with respect to Kirchoff's Law instead uses the bi-directional reflectance factor (normalized to a solar incidence of 30° and emission of 0°) as a simplification, similar to previous work[7,11]. To illustrate

the effects of this assumption, we used the phase function typically applied to M^3 data[46] to derive directional-hemispherical reflectance from example M^3 bi-directional reflectance spectra of mare and highlands surfaces. Using Kirchhoff's Law, the directional-hemispherical reflectance was used to determine emissivity and modeled emitted radiance (εI_e from Eq. 5) was subtracted from the measured radiance. The resulting corrected reflectance (R_c) show small changes (<0.003 in reflectance) and no significant change in the relative strength of the 3μm absorption (Fig. S8).

Model Uncertainties: Use of a 20° RMS slope distribution with this model predicts radiance values that closely match LRO Diviner observations. As an example, we compare the model to diurnal Diviner measurements of a mare surface near 0°N, 306°E[10]. Measured–modeled 40 μm brightness temperatures (Diviner Channel 7) have a standard deviation of 1.2K between 0700H and 1700H. This is reduced to 0.7K between 0900H and 1500H, where the magnitude of the correction is greater than at other times of day. For the same data, measured–modeled brightness temperature differences (8–40μm; Diviner Channels 4 and 7) have a standard deviation of 0.5 K (Fig. S6). The model closely predicts the measured Diviner lunar radiance over wide wavelength ranges and under a wide variety of illumination conditions.

We can more directly test the updated M^3 thermal correction by comparing the corrected data using spatially coincident Diviner measurements acquired at nearly the same local time. Under conditions of low solar incidence, rough surfaces are nearly isothermal, and consequently, Diviner measurements acquired near 8 μm wavelengths will have nearly the same brightness temperatures at M^3 wavelengths, near 3 μm. These conditions are also not particularly sensitive to surface roughness and show little difference in anisothermality for a wide range of RMS slope distributions (Fig. S6). For this comparison, we used Diviner measurements from LRO orbit 31908 and M^3 image M3G20090609T183254. To account for slight differences in solar distance and incidence angle between the M^3 and Diviner observations, thermophysical modeling predicts the M^3 surface

temperature to be +1.88 K relative to the Diviner measurements. This difference was applied to the Diviner data for this comparison.

For this example, modeled temperatures are an average of 0.1 K lower than Diviner 8 μm (Channel 4) brightness temperatures, with a standard deviation of 1.0 K. Much of the scatter between the two datasets occurs at sharp topographic boundaries, where incorrect knowledge of slope orientation can lead to incorrect temperature modeling. Most examples shown in this work avoided these areas. By comparison, the M^3 Level 2 derived temperatures average 9.7 K lower than the Diviner temperatures.

Figure S9 shows spectra from two topographically uniform areas corrected for thermal emission using the thermal roughness model described here, Diviner 8 μm temperatures, and the original M^3 Level 2 derived temperatures. In the two cases shown, the model predicts 3 μm brightness temperatures +0.7 and –0.3 K relative to the Diviner temperatures, resulting in differences of ±1% in normalized reflectance at 3 μm. For the same locations, the M^3 Level 2 data are –11.4 and –9.4 K relative to the Diviner temperatures. These lower temperatures in the M^3 Level 2 data cause an under-correction of the spectra, resulting in the lack of a distinct 3 μm absorption.

Data Availability

All data used in this work are available at the Planetary Data System. Specifically, LRO Diviner data are available at http://pds-geosciences.wustl.edu/missions/lro/diviner.htm. M^3 radiance and Level 2 reflectance data are available at https://pds-imaging.jpl.nasa.gov/volumes/m3.html. Diviner Channel 4 data were used from LRO orbit 31908 for the locations coincident with the M^3 spectra shown in Fig. S7. All M^3 image ID's, samples, and line numbers used in this work are listed in Table S1.

Code Availability

Model results and computer code that support the findings of this study are available from the corresponding author upon request.

Methods References

[39] Barker, M. K. et al. A new lunar digital elevation model from the Lunar Orbiter Laser Altimeter and SELENE Terrain Camera. *Icarus*, **273**, 346-355 http://dx.doi.org/10.1016/j.icarus.2015.07.039 (2016).

[40] Scholten, F., J. et al. GLD100: The near-global lunar 100 m raster DTM from LROC WAC stereo image data. *J. Geophys. Res.*, **117** (E12) http://dx.doi.org/10.1029/2011JE003926 (2012).

[41] Keihm, S. J. Interpretation of the lunar microwave brightness temperature spectrum - Feasibility of orbital heat flow mapping. *Icarus*, **60** 568-589 http://dx.doi.org/10.1016/0019-1035(84)90165-9 (1984).

[42] Vasavada, A. R. et al. Lunar equatorial surface temperatures and regolith properties from the Diviner Lunar Radiometer Experiment. *J. Geophys.Res.*, **117** (E12) http://dx.doi.org/10.1029/2011JE003987 (2012).

[43] Helfenstein, P. & Shepard, M. K. Submillimeter-Scale Topography of the Lunar Regolith. *Icarus*, **141**, 107-131 http://dx.doi.org/10.1006/icar.1999.6160 (1999).

[44] Shepard, M. K., Brackett, R. A., & Arvidson, R. E. Self-affine (fractal) topography: Surface parameterization and radar scattering. *J. Geophys. Res.*, **100**, 11709-11718 http://dx.doi.org/10.1029/95JE00664 (1995).

[45] Smith, B. G. Lunar Surface Roughness: Shadowing and Thermal Emission. *J. Geophys.Res.*, **72**, 4059-4067 (1967).

[46] Besse, S., et al. A visible and near-infrared photometric correction for Moon Mineralogy Mapper (M3), *Icarus*, **222**, 229–242 http://dx.doi.org/10.1016/j.icarus.2012.10.036 (2013).

[47] Logan, L. & Hunt, G. R. Emission spectra of particulate silicates under simulated lunar conditions.

J. Geophys. Res., **75**, 6539-6548 http://dx.doi.org/10.1029/JB075i032p06539 (1970).

[48] Henderson, B. G., Lucey, P. G., & Jakosky, B. M. New laboratory measurements of mid-IR emission spectra of simulated planetary surfaces. *J. Geophys. Res.*, **101**, 14969-14975 http://dx.doi.org/10.1029/96JE01089 (1996).

[49] Donaldson Hanna, K. L. et al. Effects of varying environmental conditions on emissivity spectra of bulk lunar soils: Application to Diviner thermal infrared observations of the Moon. *Icarus*, **283**, 326-342 http://dx.doi.org/10.1016/j.icarus.2016.05.034 (2017).

[50] Salisbury, J. W., Murcray, D. G., Williams, W. J., & Blatherwick, R. D. Thermal infrared spectra of the Moon. *Icarus*, **115**, 181-190 http://dx.doi.org/10.1006/icar.1995.1087 (1995).

[51] Greenhagen, B. T. et al. (2010) Global Silicate Mineralogy of the Moon from the Diviner Lunar Radiometer. *Science*, **329** 1507-1509 http://dx.doi.org/150710.1126/science.1192196 (2010).

[52] Shkuratov, Y., et al. (2011) Optical measurements of the Moon as a tool to study its surface. *Planet. Space Sci.,* **59**, 1326-1371 http://dx.doi.org/10.1016/j.pss.2011.06.011.

[53] Nicodemus, F. E. (1965) Directional reflectance and emissivity of an opaque surface. *App. Optics*, **4**, 767-775, http://dx.doi.org/10.1364/AO.4.000767.

Figures

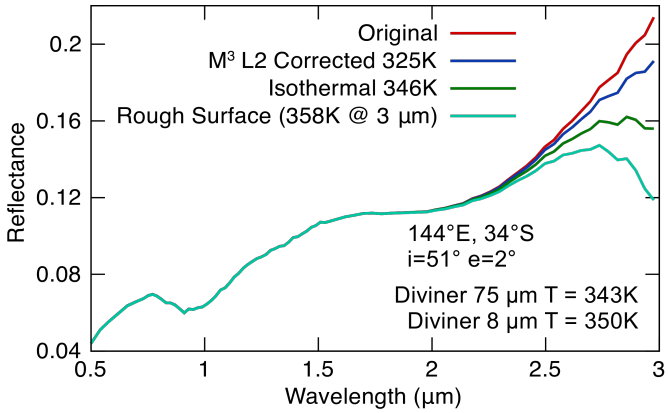

Figure 1. Example spectra showing the effects of various thermal corrections on the shape and depth of the 3 μm absorption. The original uncorrected spectrum (red) and the M^3 Level 2 thermally corrected (blue) spectra show little evidence for a 3 μm absorption. Thermal corrections using radiative equilibrium, but neglecting surface roughness (green) predict surface temperatures comparable to LRO Diviner measurements, but fail to predict the expected higher brightness temperatures at shorter wavelengths present in both Diviner data and the roughness model (cyan). Data are from M^3 image M3G20090125T172601.

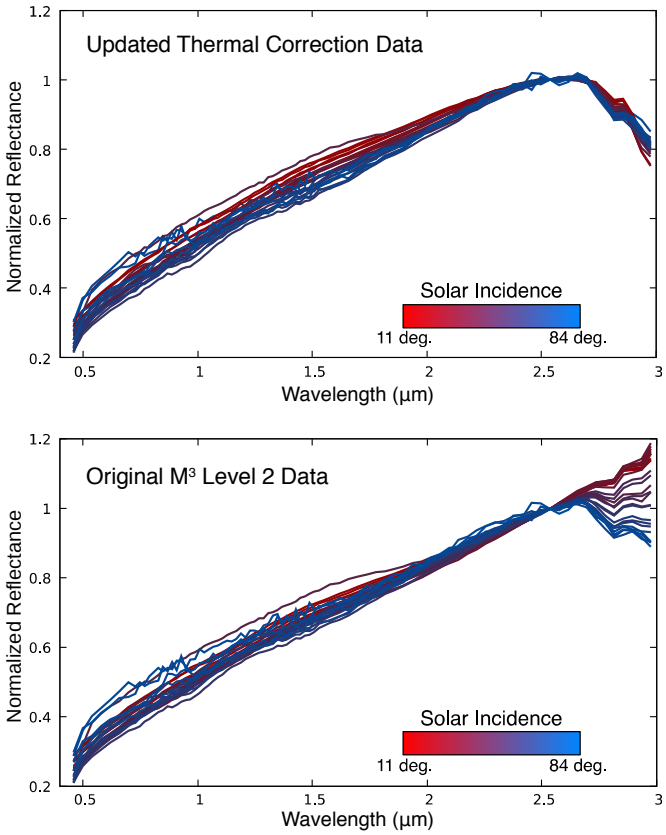

Figure 2. Normalized reflectance of lunar highlands surfaces over a range of solar incidence angles (11–84°). The top plot shows spectra corrected for thermal emission using the roughness and thermal emission model with derived 3 μm brightness temperatures from 385 to 275K. The bottom plot shows the M^3 Level 2 thermally corrected data for the same locations with derived surface temperatures of 353 to 0 K (Table S1).

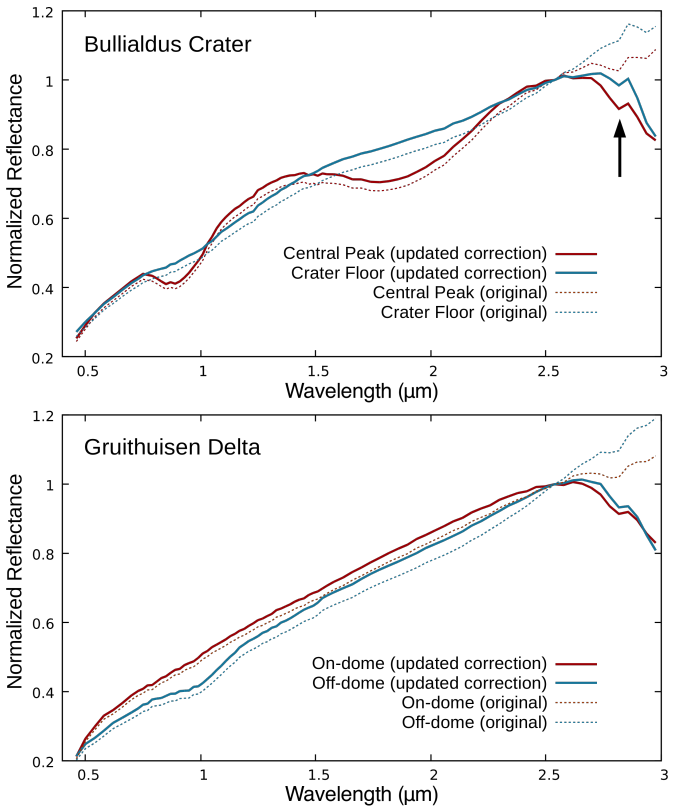

Figure 3. M^3 normalized reflectance spectra of the central peak and crater floor of Bullialdus Crater (top) and Gruithuisen Delta dome (bottom). Despite differences in the prominence of the minor 2.82 μm absorption (denoted by the arrow), the strength of the broad 3 μm absorption is comparable between the two surfaces. The spectra of Guithuisen Delta dome and nearby mare surfaces show similar 3 μm absorptions despite differences in composition and albedo (Table S1).

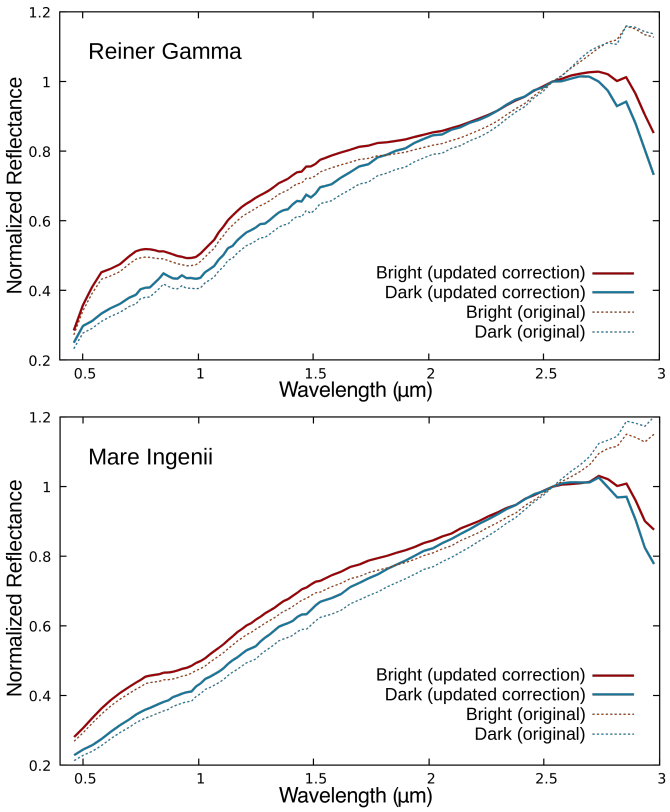

Figure 4. Reiner Gamma and Mare Ingenii lunar swirl region bright (red) and dark (blue) surface reflectance spectra. Dark surfaces have consistently deeper 3 μm absorptions than bright surfaces within lunar swirl features.

Supplementary Material to Widespread distribution of OH/H_2O on the lunar surface inferred from spectral data, by J.L. Bandfield et al.

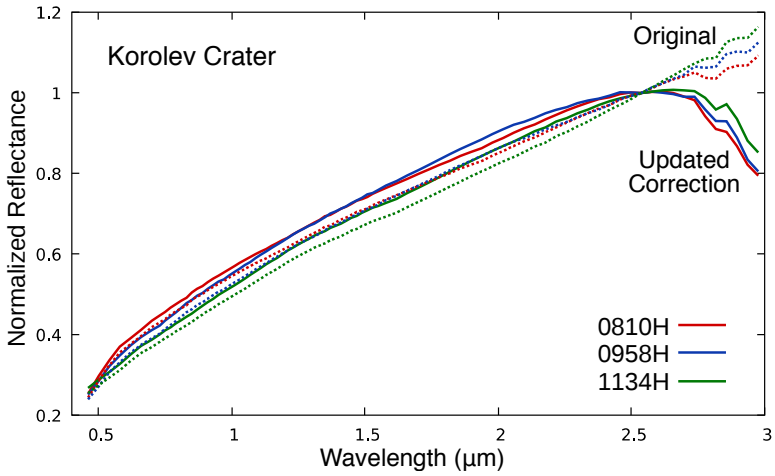

Supplementary Figure S1. Original (dashed lines) and updated (solid lines) M^3 thermally corrected spectra for a location within Korolev Crater acquired at local times from 0810H to 1134H. Although some variation is present in the updated correction spectra, the prominent 3μm absorption is present in all cases, even near local noon.

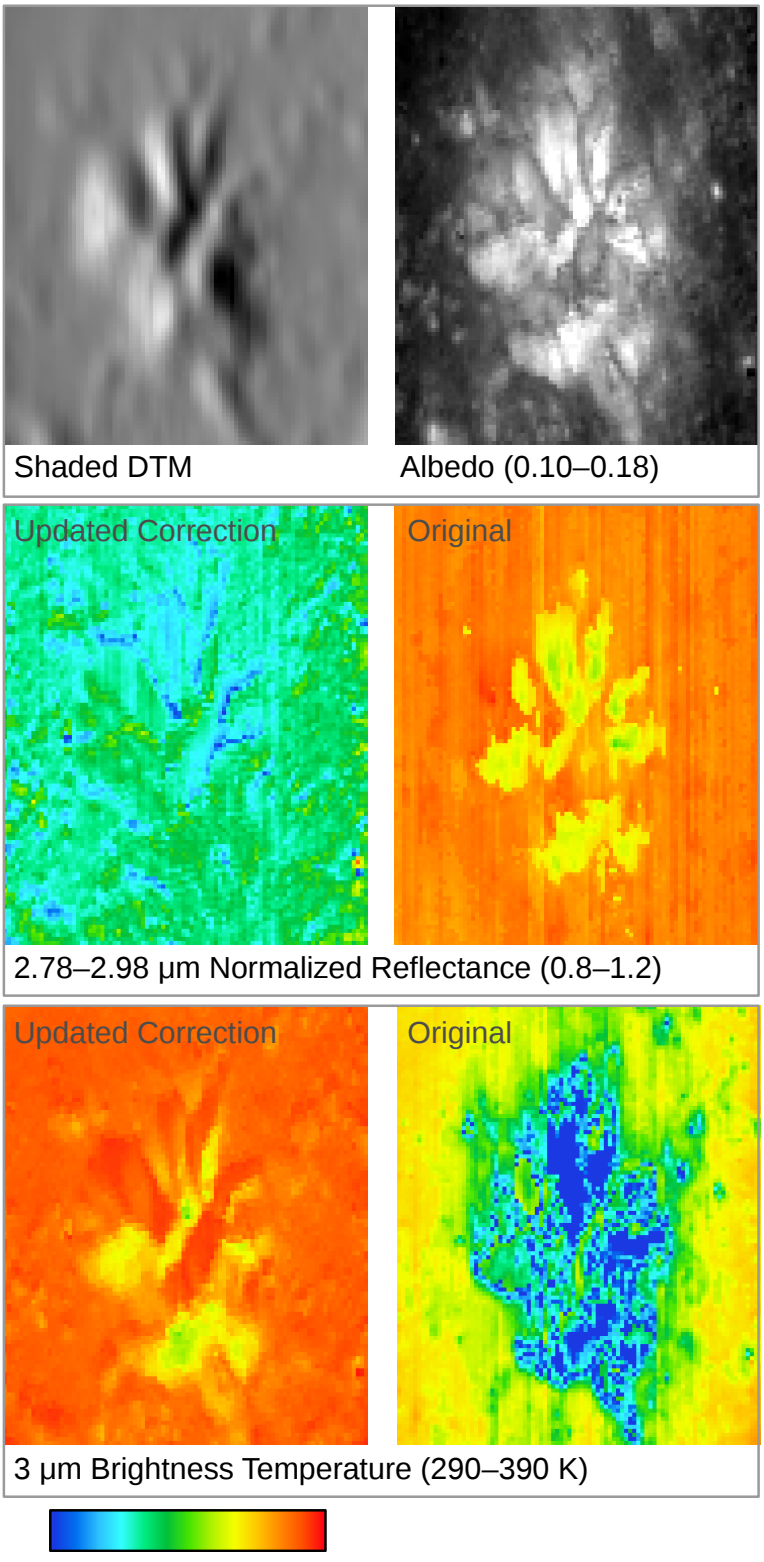

Supplementary Figure S2. Images covering the central peak and crater floor of Bullialdus Crater (M^3 image M3G20090610T070604; lines 15966–16074, samples 62–151). (top left) Shaded relief image derived from LOLA Kaguya digital elevation model. (top right) Broadband albedo used for the thermal

emission and roughness modeling. (middle left and right) 2.78–2.98 μm reflectance normalized against 2.54 μm. The original data have a much shallower absorption with deeper features associated with higher albedo surfaces. The updated data (left) show similar spectral features, regardless of location, except artifacts caused by mis-registration of the topographic data with the M^3 data (linear blue features in the image). (bottom left and right) Derived 3 μm brightness temperatures (left) and surface temperatures (right) used for the thermal correction. The updated thermal model averages 46 K higher throughout the image, resulting in a much greater predicted thermal emission and deeper 3 μm spectral features.

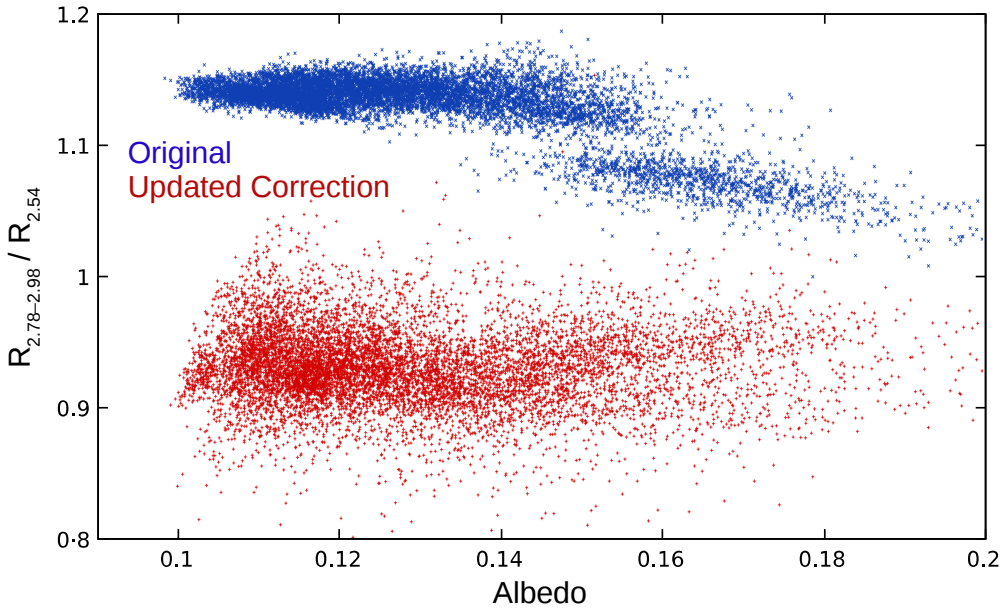

Supplementary Figure S3. Scatterplot showing the depth of the 2.78–2.98 μm absorption relative to surface albedo. The data are the same as shown in the middle images in Fig. S1. The original M^3 Level 2 thermally corrected data (blue) show a much shallower (or non-existent) 3 μm absorption with two distinct populations. The lower reflectance values that correspond to higher albedos are typically associated with the Bullialdus Crater central peak. This separate population disappears in the updated thermally corrected data (red; see also Fig. S1). The updated correction has a greater scatter due to imprecise registration between the topographic and the M^3 data. This results in errors in slope orientation that influence modeled surface temperatures and the resulting magnitude of the thermal correction.

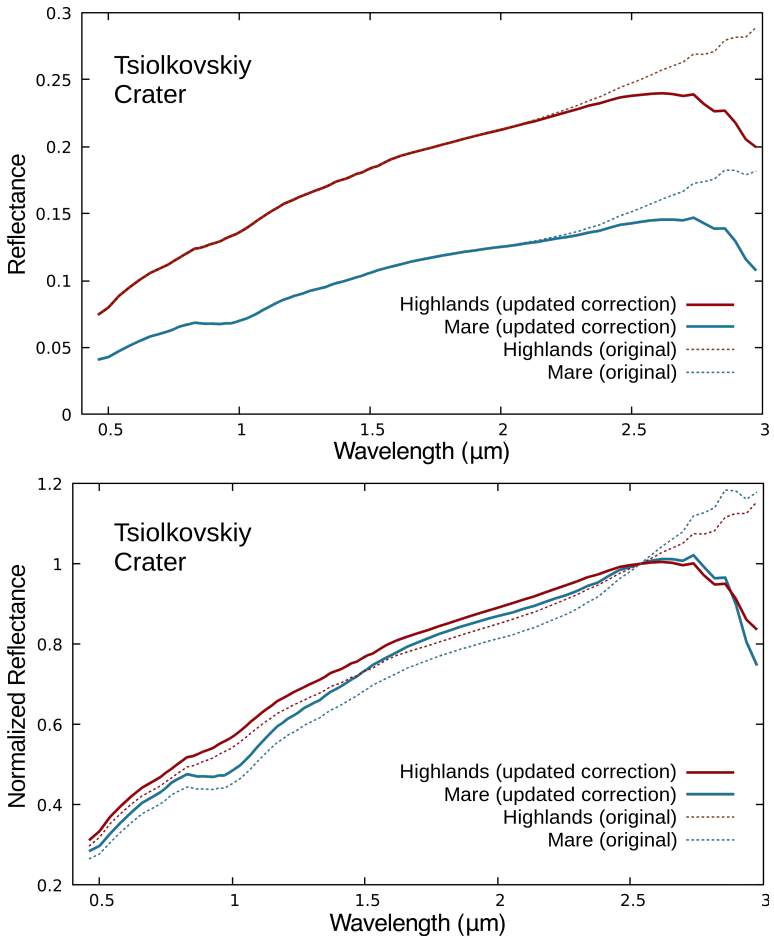

Supplementary Figure S4. Mare and highlands surface reflectance spectra within and near Tsiolkovkiy Crater. Mare surfaces have a slightly, but consistently deeper 3 µm absorption than adjacent highlands surfaces.

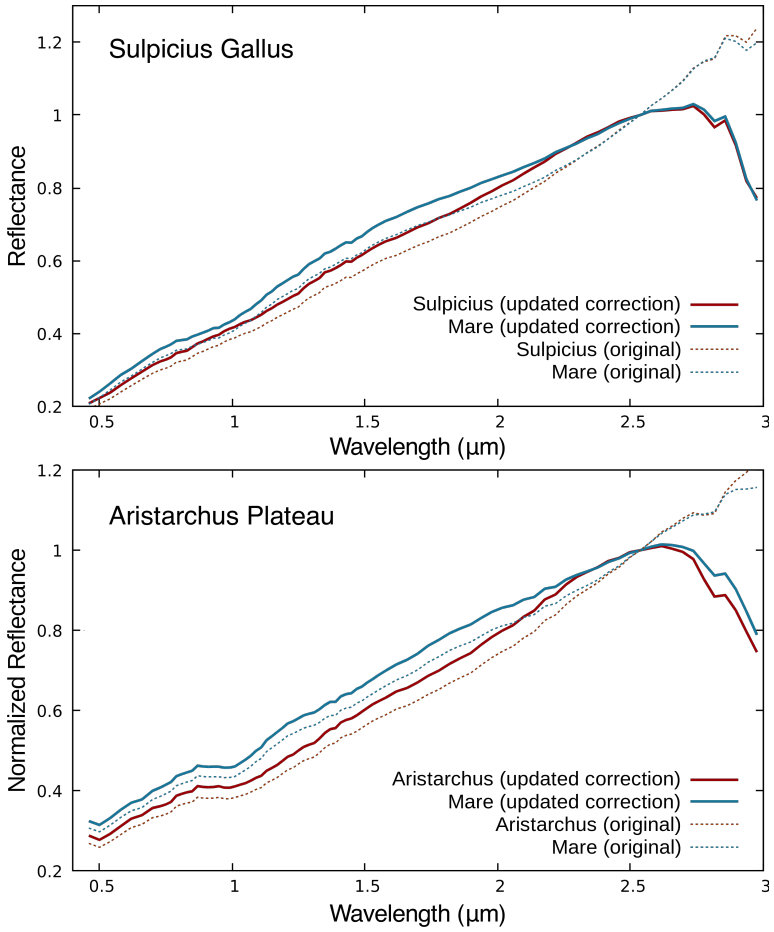

Supplementary Figure S5. Pyroclastic deposit surface reflectance spectra (red) compared with adjacent mare surface spectra (blue). Although some relative variation in the strength of the 3 μm absorption is present, there is no clear systematic difference between the two surface compositional types.

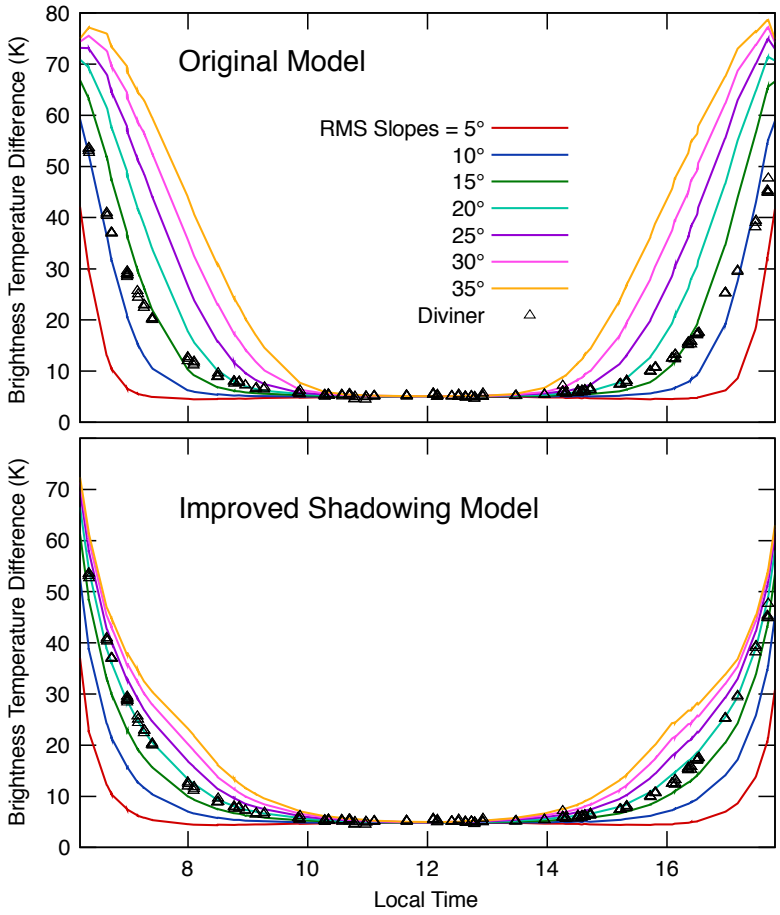

Supplementary Figure S6. Equatorial mare Channel 4 (centered near 8μm) minus Channel 7 (centered near 40μm) brightness temperature differences. The black triangles are the Diviner measurements and are the same data used in Bandfield et al. (2015)[10]. Colored lines show roughness thermal model results for a range of RMS slope distributions. The top plot shows the modeling used in previous work and the bottom plot shows the improved modeling used for this work. Data sensitivity to roughness becomes pronounced at solar incidence angles greater than ~30° (local times outside of 1000H to 1400H at the equator). The model matches the data at an RMS slope distribution of 20°, which is tha value used for this work. Small irregularities in the model lines are due to differences in solar distance between individual Diviner observations.

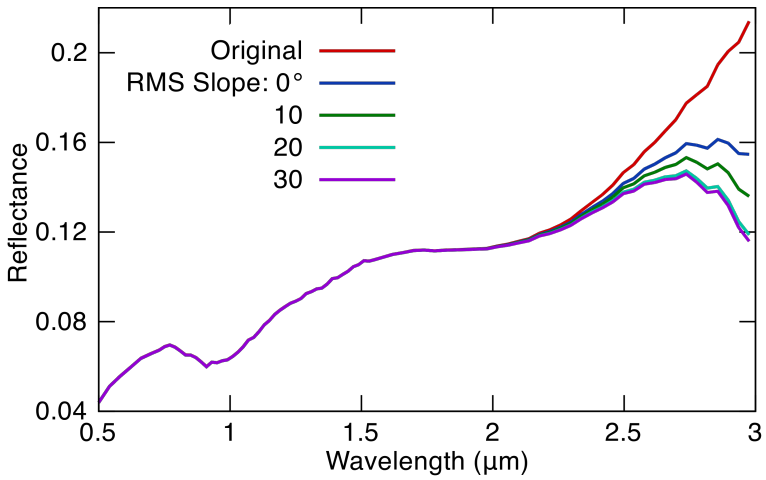

Supplementary Figure S7. Effects of surface roughness modeling on the thermally corrected M^3 spectra. At a solar incidence angle of 51°, surface roughness results and a wide variety of surface temperatures for sunlit and shadowed surfaces, resulting in a higher emitted radiance at short wavelengths near 3 μm. Removal of the excess emitted radiance results in a more prominent 3 μm absorption. The lunar surface is consistent with RMS roughness values of ~20°. The spectra shown here are from M^3 image M3G20090125T172601 and are the same data as that used in Fig. 1.

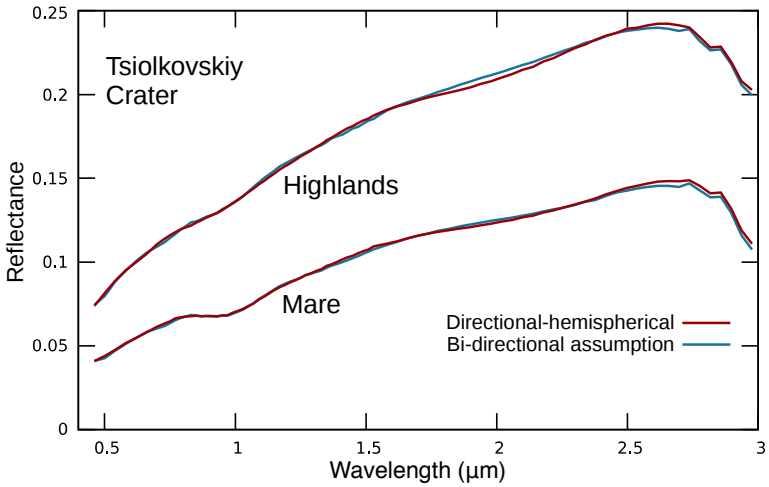

Supplementary Figure S8. Thermally corrected data from example mare and highlands surfaces (Fig. S4) showing the difference between using directional-hemispherical and bi-directional reflectance for emissivity determination for thermal removal. Although directional-hemispherical reflectance in this case is 9–14% higher than bi-directional reflectance, the resulting effect on emitted radiance and thermally corrected reflectance is small.

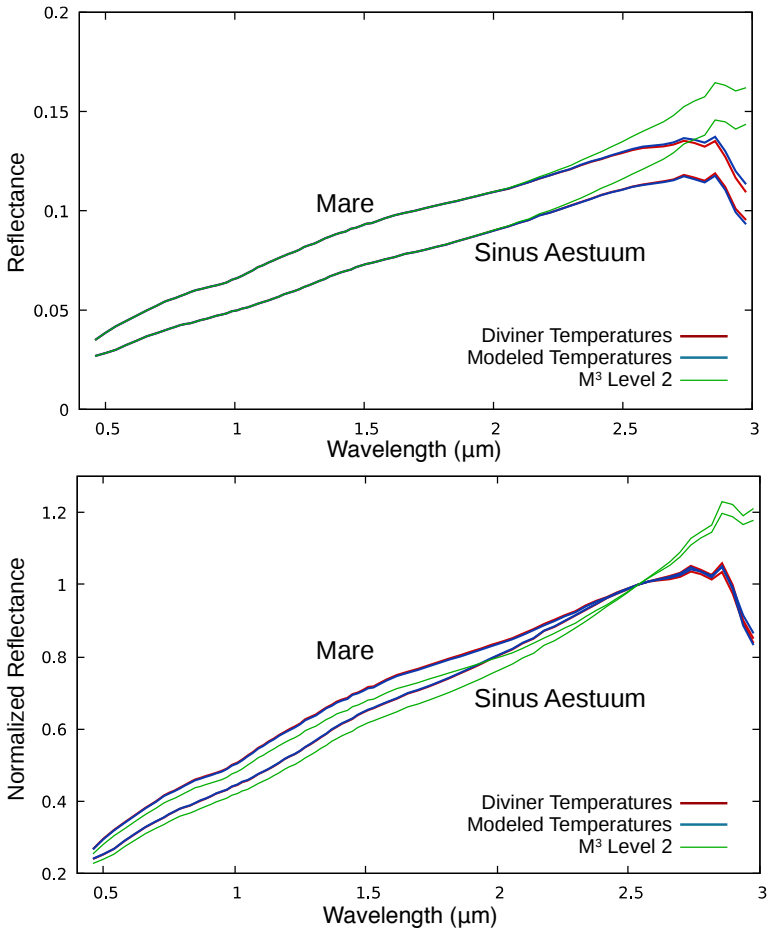

Supplementary Figure S9. Comparison of M^3 spectra corrected using temperatures derived from Diviner observations (red), the updated model (blue), and the original M^3 Level 2 thermally corrected spectra (green). Under the conditions of low solar incidence where anisothermality due to surface roughness is minimized, the modeled temperatures closely match the Diviner measurements and produce similar spectra with prominent 3 μm absorptions.

Supplementary Table S1. Image ID's, samples, line numbers, average geometry, and derived information for spectral plots shown in Figures 1, 2-4 and Supplementary Figures 2 and 3. All data were selected for surfaces with consistent and low slopes (<10°) to avoid potential mis-registration problems with the topographic data.

Label	Samples	Lines	Original T(K)	Updated 3μm T(K)	Solar Incidence	Phase Angle	Albedo	Latitude (N)	Longitude (E)
Aristarchus	**M3G20090418T174554**								
Aristarchus	125-160	11770-11800	306.6	338.5	61.0	60.9	0.06	28.54	310.49
Mare	125-160	11001-11050	312.8	336.3	61.7	62.0	0.07	32.49	310.44
Sulpicius Gallus	**M3G20090608T000122**								
Sulpicius Gallus	274-285	14065-14125	372.6	385.6	21.8	23.7	0.06	20.42	9.37
Mare	274-285	13351-13410	370.3	382.9	24.7	27.1	0.07	23.83	9.39
Gruithuisen	**M3T20090418T020644**								
On-dome	54-64	10351-10360	0.0	332.2	62.9	54.3	0.13	36.72	319.32
Off-dome	54-64	10405-10435	301.5	339.5	61.4	54.1	0.08	36.10	319.30
Bullialdus Crater	**M3G20090610T070604**								
Central Peak	100-105	15998-16003	16.3	376.3	17.7	23.3	0.18	-20.71	337.68
Crater Floor	100-105	16095-16101	362.0	380.7	21.4	23.7	0.11	-21.17	337.67
Reiner Gamma	**M3G20090210T0330524**								
Bright	115-125	8960-8970	330.2	347.0	55.9	53.1	0.10	7.74	300.96
Dark	115-125	8871-8880	335.8	350.4	56.1	53.0	0.06	8.20	300.97
Mare Ingenii	**M3G20090623T135841**								
Bright	18-24	3701-3708	351.8	369.4	35.2	37.2	0.12	-33.73	162.78
Dark	18-24	3513-3520	359.0	374.6	34.2	36.6	0.07	-33.06	162.78
Mare/Highlands	**M3G20090529T183825**								
Mare	99-139	16888-16928	364.6	379.8	26.9	32.6	0.09	-18.93	129.78
Highlands	99-139	16734-16773	314.8	370.2	28.7	32.0	0.16	-18.19	129.78
Korolev Crater									
0800H (M3G20090814T102823)	134-148	15667-15681	0.0	341.6	55.0	56.4	0.14	-4.38	200.50
1000H (M3G20090718T014252)	44-58	19200-19214	338.7	373.0	29.6	24.5	0.14	-4.38	200.50
1200H (M3G20090620T181042)	76-90	17948-17962	351.8	387.6	6.1	6.2	0.11	-4.38	200.50
Sinus Aestuum	**M3G20090609T183254**								
Sinus Aestuum	165-173	17154-17161	383.1	392.2	8.0	7.9	0.05	6.13	345.14
Mare	175-186	17692-17701	378.5	390.6	8.2	5.9	0.07	3.55	345.26
Solar Incidence Transect	**M3G20090529T183825 (1-11) / M3G20090213T001153 (12-25)**								
1	176-189	12016-12027	353.1	385.0	11.5	14.8	0.13	4.35	130.33
2	121-141	11341-11360	349.5	382.2	15.0	18.4	0.14	7.53	129.85
3	106-117	11556-11569	353.1	381.4	18.5	19.9	0.13	6.51	129.67
4	7-23	15060-15077	346.8	379.8	19.9	32.5	0.13	-10.24	128.79
5	54-66	16119-16133	346.5	378.0	24.3	32.9	0.12	-15.28	129.23
6	184-190	17917-17924	319.6	370.7	30.8	33.9	0.15	-23.83	130.45
7	212-227	18794-18813	312.0	368.9	33.2	36.6	0.14	-28.05	130.81
8	207-215	19747-19757	301.2	364.2	37.4	41.1	0.14	-32.61	130.75
9	46-58	20718-20730	279.4	359.1	42.6	50.7	0.13	-37.31	129.03
10	91-98	21730-21740	18.1	353.5	46.1	53.5	0.14	-42.15	129.47
11	125-137	22636-22650	4.7	343.9	50.7	56.4	0.17	-46.51	129.90
12	88-95	18063-18070	0.0	343.0	54.1	53.6	0.18	-4.86	263.11
13	211-230	16961-16980	31.9	340.9	56.9	63.4	0.13	0.75	263.72
14	191-210	12401-12420	0.0	338.2	58.4	64.7	0.13	24.10	263.62
15	171-190	10711-10730	0.0	330.5	62.7	65.6	0.13	32.74	263.50
16	151-170	8671-8690	0.0	321.0	67.5	67.7	0.13	43.16	263.35
17	161-180	7321-7350	1.1	316.7	69.6	71.2	0.12	50.02	263.39
18	33-39	9-13	0.0	309.0	70.1	80.3	0.18	87.30	245.25
19	121-140	3581-3600	0.0	308.3	71.9	77.3	0.15	69.13	262.63
20	216-235	6016-6035	0.0	307.4	72.9	77.9	0.14	56.70	263.88
21	101-120	4801-4820	0.0	298.2	77.0	72.9	0.13	62.90	262.62
22	69-78	682-690	0.0	289.9	77.8	81.1	0.19	83.94	257.41
23	91-110	2526-2545	0.0	288.2	80.2	78.0	0.14	74.51	261.71
24	65-80	745-760	0.0	281.6	80.8	80.8	0.18	83.60	257.68
25	26-45	1851-1870	12.1	275.1	84.0	75.3	0.14	77.96	259.52